

Towards cosmological inference on unlabeled out-of-distribution HI observational data

Sambatra Andrianomena^{1,2*} and Sultan Hassan^{2,3†}

¹*SARAO, Liesbeek House, River Park Liesbeek Parkway, Settlers Way, Mowbray, Cape Town, 7705*

²*Department of Physics & Astronomy, University of the Western Cape, Bellville, Cape Town 7535, South Africa and*

³*Center for Cosmology and Particle Physics, Department of Physics,
New York University, 726 Broadway, New York, NY 10003, USA*

(Dated: November 19, 2024)

We present an approach that can be utilized in order to account for the covariate shift between two datasets of the same observable with different distributions, so as to improve the generalizability of a neural network model trained on in-distribution samples (IDs) when inferring cosmology at the field level on out-of-distribution samples (OODs) of *unknown labels*. We make use of HI maps from the two simulation suites in CAMELS, IllustrisTNG and SIMBA. We consider two different techniques, namely adversarial approach and optimal transport, to adapt a target network whose initial weights are those of a source network pre-trained on a labeled dataset. Results show that after adaptation, salient features that are extracted by source and target encoders are well aligned in the embedding space, indicating that the target encoder has learned the representations of the target domain via the adversarial training and optimal transport. Furthermore, in all scenarios considered in our analyses, the target encoder, which does not have access to any labels (Ω_m) during adaptation phase, is able to retrieve the underlying Ω_m from out-of-distribution maps to a great accuracy of R^2 score ≥ 0.9 , comparable to the performance of the source encoder trained in a supervised learning setup. We further test the viability of the techniques when only a few out-of-distribution instances are available and find that the target encoder still reasonably recovers the matter density. Our approach is critical in extracting information from upcoming large scale surveys.

I. INTRODUCTION

Previous studies showed that HI intensity mapping technique [1, 2], which consists of collecting the combined emission of HI galaxies of large scale structure at 21cm wavelength, can be used as a powerful probe to constrain cosmological parameters (e.g. [3, 4]). Several ongoing and upcoming HI experiments are expected to provide more insights into the late time acceleration of the Universe, such as Square Kilometre Array (SKA) [5], BINGO [6], the Canadian Hydrogen Intensity Mapping Experiment (CHIME) [7], Five-hundred-meter Aperture Spherical radio Telescope (FAST) [8, 9], Hydrogen Epoch of Reionization Array (HERA) [10], MeerKAT Large Area Synoptic Survey (MeerKLASS) [11].

By utilizing 21 cm power spectrum in a Bayesian framework (such as Monte Carlo Markov Chain), various studies showed that constraining cosmological parameters to a promising accuracy is achievable (e.g. [12] [13]). Nevertheless, power spectrum analysis are prone to information loss since it mainly encodes the mean distribution of matter clustering at different k modes. Previous works for instance had to resort to high order statistics (such as bispectrum) [14, 15] to further capture the non-gaussianity in 21 cm signal in such a way as to break degeneracies between parameters, improving the constraints obtained from HI intensity mapping surveys [16]. In order to circumvent the challenges that come with modeling physics at non-linear scales, and to minimize the signal loss inherent in power spectrum analyses, extracting the parameters at the field level (i.e. two dimensional maps or three dimensional data cube) using deep learning looks very

promising. For instance, [17] trained a convolutional neural network (CNN) to predict astrophysical parameters from 2D HI maps to a great accuracy; [18] made use of HI maps from CAMELS dataset [19] to train a Masked Autoregressive Flow (MAF) [20] which successfully learned the HI data distribution so as to able to generate new images mimicking the training data. By conditioning on the matter density (Ω_m) and the amplitude of the density fluctuations (σ_8), and using the marginal likelihood which is obtained by inverting the flow, the model in [18] can infer the underlying cosmology of HI maps. [21] also demonstrated that the constraints on the cosmology and astrophysics improved by combining HI maps with the gas density and amplitude of the magnetic fields maps at the input of their CNN model which also output the predictive uncertainties on each inferred parameter by using Bayesian approximation. [22] highlighted the fact that the performance of their deep networks degraded when trained to recover cosmology and astrophysics from noisy (more realistic) HI maps.

Foreground noise, whose dominant component is the galactic synchrotron emission, buries the cosmological signal, which is challenging to information extraction. [23], for instance, modeled the noise contamination in Fourier space before removing it. [24] prescribed a unified matrix-based approach to subtract the foregrounds and estimate the power spectrum of the signal. Provided the smoothness in frequency of the contaminating noise, [25] opted for a blind signal separation technique which consists of removing the most dominant component of the foregrounds by using Principal Component Analysis (PCA)[26]. Deep learning based methods have also been explored in order to clean the noisy maps. In their analyses, [27] built a denoising U-net model to predict the cosmological signal from PCA-reduced maps, in other words maps whose dominant contributions were removed using PCA.

* hagatiana.andrianomena@gmail.com

† sultan.hassan@nyu.edu

Despite various noise prescriptions adopted when simulating HI maps for a given survey, the mock datasets for training neural network models will always be different from the real datasets collected from the experiment. This data shift, i.e. difference between the distributions of real and simulated data, is most likely to hit the performance of a deep learning model trained on the simulated maps when tested on dataset from surveys. In order to overcome this issue, domain adaptation (DA) techniques, which mainly consist of learning robust representations that are invariant to domain shift, have been proposed (e.g. see [28–30]). Various DA approaches have been explored to address issues in Astronomy and Astrophysics. [31] considered three different deep unsupervised domain adaptation methods to improve the robustness of their deep network in preparation for Imaging Atmospheric Cherenkov Telescopes event reconstruction. Semi-supervised universal DA was used to account for the varying systematics in different galaxy surveys within the context of galaxy morphology classification and anomaly detection [32] (see also [33] for the use of DA galaxy morphology classification). [34] opted for Kullback–Leibler Importance Estimation Procedure [35] to constrain star formation history. [36] used Maximum Mean Discrepancy (MMD) [37] and Domain Adversarial Neural Networks (DANN) [28] to improve the performance of their network in classifying galaxy mergers.

This far, several deep networks have been successfully trained on HI mock data to recover the underlying cosmology, however there are two issues that need to be addressed in a real world scenario

- the complexity of noise modeling in HI experiments leads to a domain shift which will negatively impact the performance of a model trained on simulated data,
- realistic scenario, i.e. HI maps from experiments, will not have labels that can be used to evaluate the model predictions.

In this proof of concept, we propose an approach that can potentially tackle those problems by making use of unsupervised domain adaptation techniques which will help improve the generalizability of a deep network model when attempting to extract cosmological information from real data of HI surveys. We present the datasets considered in our analyses in §II, and describe the two approaches in §III. We show the results in §IV and conclude in §V.

II. DATA

In this work we consider the multifield dataset [38] from the CAMELS Project [19, 39]. CAMELS uses two different state-of-the-art hydrodynamic simulation suites, IllustrisTNG [40] and SIMBA [41], to generate hundreds of thousands of 2D field maps which correspond to a region of $25 \times 25 (h^{-1}\text{Mpc})^2$ at $z = 0$. The maps, with a resolution of 256×256 pixels, were obtained by varying the cosmology (Ω_m , σ_8) and the astrophysics composed of the stellar feedbacks ($A_{\text{SN}1}$, $A_{\text{SN}2}$) and active galactic nuclei (AGN) feedbacks ($A_{\text{AGN}1}$, $A_{\text{AGN}2}$).

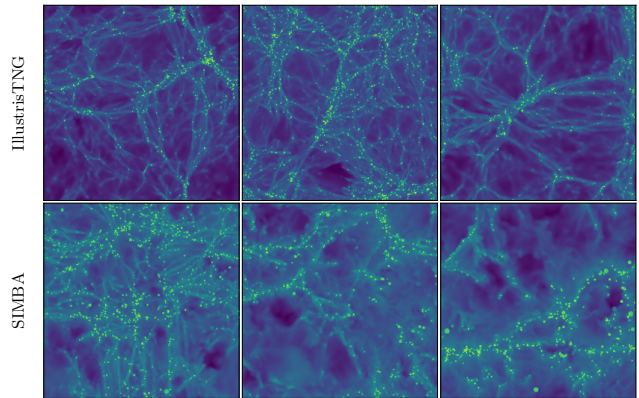


FIG. 1. Random samples of HI maps from IllustrisTNG and SIMBA are shown in the top and bottom panels respectively. The color coding in both datasets is set to be the same for a better comparison. This figure shows that the HI maps are visually very different in the two simulations.

To mimic the source and target domains in our analyses, we make use of the HI maps from SIMBA and IllustrisTNG which are two datasets generated by two different distributions owing to the different ionizing background adopted in each suite (SIMBA uses [42] whereas IllustrisTNG opts for [43]). We present in Figure 1 samples from both datasets. All the topological features, e.g. voids, filaments and halos, are noticeable in both types of samples, but the clear difference lies in the image texture. The small scale features in SIMBA (see bottom panels in Figure 1) tend to be a bit blurry in comparison with those of IllustrisTNG (see top panels in Figure 1). To further highlight the difference between the two datasets, we plot in Figure 2, the distributions of the mean value of the pixels of the two domain images. After normalizing the pixel values in all maps to $[0,1]$, each curve is obtained by averaging the pixel value distribution of all the images in each domain. Red and blue solid lines denote SIMBA and IllustrisTNG respectively. There is a clear shift between the two distributions in Figure 2, suggesting that the samples in one dataset are viewed as out-of-distribution samples of the other. We first treat SIMBA and IllustrisTNG as the source and target domains respectively, then vice versa. In what follows, unless otherwise state, we will use source and target domain maps/data interchangeably with in-distribution and out-of-distribution maps/data respectively.

In this regression task, the networks are trained to extract the underlying cosmology (Ω_m and σ_8) of the maps, while marginalizing over the astrophysical parameters. The prior ranges of the labels, i.e. the cosmological parameters, are the same in both domains, the matter density Ω_m within $[0.1, 0.5]$ and the amplitude of the density fluctuations σ_8 within $[0.6, 1.0]$ [38]. We select 12,000 pairs of {map, label} from each domain to train the two networks, and 1,500 of unseen instances from both domains are used for testing. It is worth noting that the labels of the target domain are not accessed during training phases, i.e. pre-training of the source network and adaptation of the target network, but are only used to as-

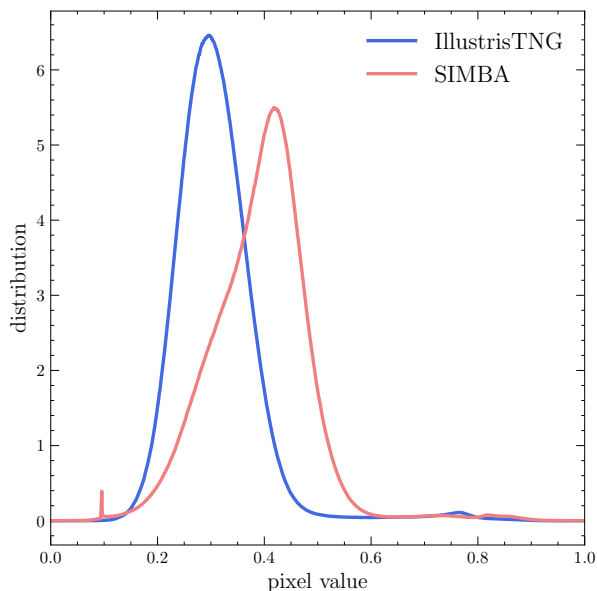


FIG. 2. Probability distribution of the pixel values of the HI maps from each simulation. Blue and red solid lines denote the distributions from IllustrisTNG and SIMBA respectively. The pixel values in all maps are normalized to $[0,1]$. This figure shows a clear distribution shift between SIMBA and IllustrisTNG at the level of HI maps.

sess the performance of the adapted target encoder.

III. METHOD

We consider two methods that have similar training steps and use the exact same source and target encoders, but are different in how the target encoder weights are updated during the adaptation phase. In the following subsections, we first provide a very brief introduction of domain adaptation, especially the case relevant to our study, and then present the two methods.

A. Domain adaptation

A domain \mathcal{D} is composed of a feature space \mathcal{X} whose elements x are in d -dimensions (i.e. $\in \mathbb{R}^d$), a label space \mathcal{Y} whose elements can be either a class label in the case of classification or a dependent variable (scalar) defined with a range (i.e. prior) in the case of regression, and finally a joint probability distribution $p(x, y)$. Since, in a supervised learning, the label is inferred from the input feature, the joint probability distribution can be written as $p(x, y) = p(y|x)p(x)$ ¹ where

¹ It can also be written as $p(x, y) = p(x|y)p(y)$ but we choose the one in the text to be consistent with a standard supervised learning setup where the aim is to predict the label.

the first term is the probability of the label given the input and the second term is known as the prior.

In general for a given supervised learning task, the test set² is assumed to be from the same distribution of the dataset³ that is used to train a model. However, in some cases during deployment of the trained model, its performance significantly degrades as the assumption is no longer valid, i.e. there is a shift between the source and target domains. The aim of domain adaptation is to minimize the generalization error of a trained model in the presence of a domain shift which can be (see [44] for a review)

- a prior shift which arises when the label distribution of the target domain differs from that of the source domain, in other words $p_S(y_S) \neq p_T(y_T)$,
- covariate shift characterized by a discrepancy between the feature space of source domain and that of the target domain, i.e. $p_S(x_S) \neq p_T(x_T)$,
- concept shift where the conditional distributions in source and target domains are different, i.e. $p_S(y_S|x_S) \neq p_T(y_T|x_T)$.

In our analyses, it assumed that *the labels of the target domain do not exist*, a case of an unsupervised domain adaptation, to mimic a real world scenario where we infer the cosmological parameters of maps from experiments using a deep learning model trained on simulated data. We also assume that the label space and the mapping between feature and label remain the same in both domains, so that we deal with a covariate shift in our investigation. These assumptions are valid since the same range of cosmological parameters (i.e. prior range) is adopted in both simulation suites ($p_S(y) = p_T(y)$), and regardless of the treatment of the baryon physics used in SIMBA and IllustrisTNG, the topological features of the maps in both cases are equally sensitive to the cosmology. We consider two approaches in our study which will be presented in the following sections.

B. Adversarial discriminative domain adaptation

We first consider an adversarial method, named Adversarial Discriminative Domain Adaptation (ADDA), which was prescribed in [45] for a classification task originally. The setup consists of feature \mathcal{X}_S and label \mathcal{Y}_S spaces of the source domain and feature \mathcal{X}_T of the target domain which is unlabeled, in other words we do not have access to the label space \mathcal{Y}_T during the training phases. The goal is to be able to predict the labels corresponding to the inputs from the target domain maps.

The idea is to first learn representations $h_S(\mathcal{X}_S)$ of the input distribution images along with a regressor \mathcal{R}_S that is used to recover the underlying cosmology (Ω_m, σ_8) of the inputs

² Or generally the target domain.

³ Or also the source domain.

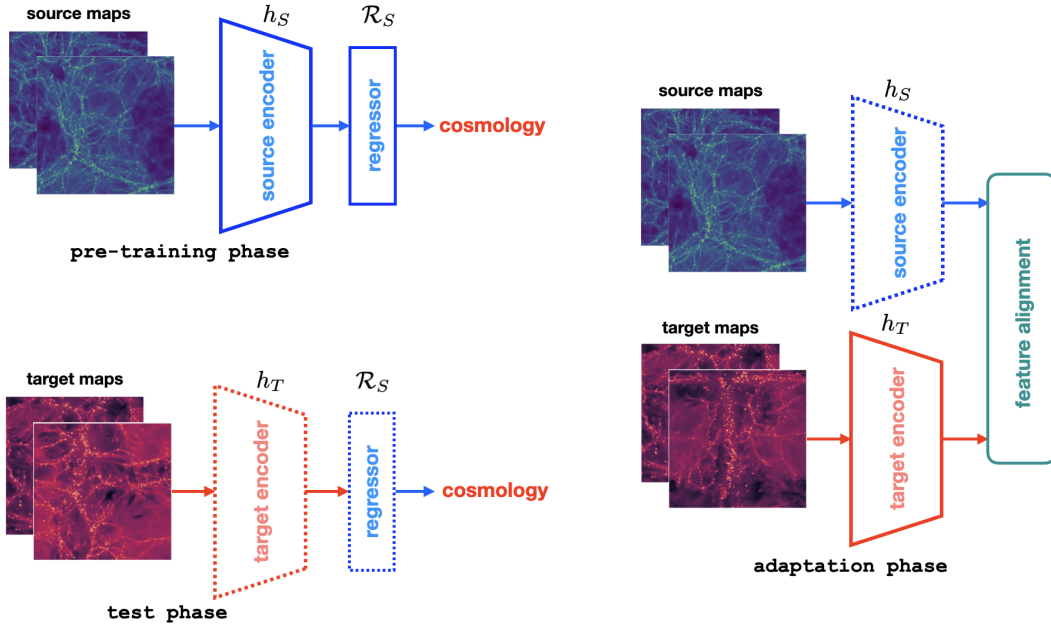


FIG. 3. Schematic view of the different phases. The source encoder and a regressor are first trained to infer underlying cosmology of in-distribution instances. At the beginning of the adaptation, the weights of the pre-trained source encoder are used to initialize the target encoder (whose architecture is identical to that of the source feature extractor). The target encoder is trained by aligning the features it extracts from the target maps with those of the source maps learned by the source encoder. Finally, during testing, the representations of the test set from the target domain, which are encoded by the trained target encoder, are fed to the regressor for inference. It is noted that the weights of a component in dashed line (blue or red) are frozen during a given phase.

(maps) in a supervised learning setup. The source encoder h_S , shown in Figure 3 (pre-training phase), has an architecture similar to a VGG feature extractor [46] composed of different stages that are built from chaining up 2 or 3 convolutional layers. The outputs of the last layer in each stage is halved using max pooling layers (with stride = 2) and from one stage to another the number of channels is doubled. A single fully connected layer constitutes a regressor \mathcal{R}_S . The loss that is considered in the pre-training phase is the same as the one used in [21]

$$\mathcal{L}_{Reg} = \frac{1}{N \times M} \sum_{i=1}^N \left[\log \left(\sum_{j=1}^M (\theta_{i,j} - \mu_{i,j})^2 \right) + \log \left(\sum_{j=1}^M ((\theta_{i,j} - \mu_{i,j})^2 - \sigma_{i,j}^2)^2 \right) \right], \quad (1)$$

where N , M , $\theta_{i,j}$, $\mu_{i,j}$ and $\sigma_{i,j}$ are the number of parameters, batch size, ground truth, prediction and standard deviation respectively. The cosmological parameters (Ω_m, σ_8) and their corresponding standard deviation are the outputs of the regressor⁴.

The adaptation phase (Figure 3) consists of training adversarially a target encoder h_T , whose architecture is identical to

that of h_S , such that the representations of target domain maps $h_T(\mathcal{X}_T)$ are well aligned with $h_S(\mathcal{X}_S)$ in a lower dimensional latent space. Initially, the weights of the pre-trained source encoder are transferred to the target encoder, in order to avoid divergence during training. During adaptation, the source encoder weights are frozen, and a discriminator \mathcal{C} , which comprises two hidden fully connected layers of 512 units each, learns to separate the two latent codes $h_S(\mathcal{X}_S)$ and $h_T(\mathcal{X}_T)$ (see Figure 3). In order to align the two different representations, the loss is composed of [45]

$$\min_D \mathcal{L}_{adv}^C = -\mathbb{E}_{x_S \sim p_S(x_S)} [\log \mathcal{C}(h_S(\mathcal{X}_S))] - \mathbb{E}_{x_T \sim p_T(x_T)} [\log(1 - \mathcal{C}(h_T(\mathcal{X}_T)))] \quad (2)$$

which is a component that is used to update the discriminator such that its ability to differentiate between the two representations improves during training, and [45]

$$\min_{h_S, h_T} \mathcal{L}_{adv}^{h_T} = -\mathbb{E}_{x_T \sim p_T(x_T)} [\log \mathcal{C}(h_T(\mathcal{X}_T))] \quad (3)$$

which is used to update to target encoder. It is worth pointing out that the target feature extractor plays a role similar to that of a generator in GANs by trying to fool the discriminator. To retrieve the cosmological information from a test set of the target domain, the pre-trained regressor \mathcal{R}^5 is fed with the

⁴ This implies that the total number of outputs of the regressor is 4.

⁵ The one used for prediction in pre-training phase.

representations extracted by the adapted network (see Figure 3 test phase).

We pre-train both the source feature extractor and regressor for 200 epochs, using Adam optimizer with learning = 0.0015 and opting for a batch size = 50. The learning rate is halved whenever the loss function does not improve over 5 epochs by using `ReduceOnPlateau`. The hyperparameters for the pre-training are based on the prescription in [21]. The adaptation phase is run for 200 epochs in the case where IllustrisTNG constitutes the out-distribution dataset, and 800 epochs when SIMBA is target domain. The reason for choosing different epochs for the two scenarios will be more apparent in §IV. The target encoder and the classifier have their own Adam optimizer with learning rates 10^{-5} and 10^{-4} respectively. The values of the learning rates are from this implementation upon which ours is based.

C. Optimal transport

Optimal Transport [47] (OT), which is an approach whose objective is to find an optimized solution to move unit mass between different distributions, can also be used to estimate the dissimilarity between two probability distributions, similar to Maximum Mean Discrepancy [37]. Generally, within the context of domain adaptation problems, OT approach consists of finding a transport map \mathcal{T} , which transforms samples from source domain to the target domain, such that the transportation cost \mathcal{C} [47]

$$\mathcal{C}(\mathcal{T}) = \int c(x, \mathcal{T}(x)) d\mu(x), \quad (4)$$

is minimized, according to [47]

$$\mathcal{T}_0 = \operatorname{argmin}_{\mathcal{T}} \int c(x, \mathcal{T}(x)) d\mu(x), \quad (5)$$

where $c(\cdot, \cdot)$ is a cost function and μ is a marginal distribution. This optimal transport problem can be framed differently as [48]

$$\gamma_0 = \operatorname{argmin}_{\gamma \in \mathbb{R}_+^{n_s \times n_t}} \int \int c(x_S, x_T) \gamma(x_S, x_T) dx_S dx_T, \quad (6)$$

where γ , known as the transport plan, is a joint probability and denotes the amount of mass to be moved between the two distributions. In the discrete case, we have that

$$\gamma_0 = \operatorname{argmin}_{\gamma \in \mathcal{B}} \sum_{i,j} \gamma_{i,j} M_{i,j}, \quad (7)$$

such that [47]

$$\mathcal{B} = \{\gamma \in \mathbb{R}_+^{n_s \times n_t} \mid \gamma \mathbf{1}_{n_s} = \mu_s, \gamma \mathbf{1}_{n_t}^T = \mu_t\}, \quad (8)$$

and $M_{i,j}$ is a metric cost matrix. To align the two different distributions of representations μ_s, μ_t of source and target

domains respectively, we minimize the Wasserstein distance [49], also known as Earth Mover’s Distance [50], given by

$$W_p(\mu_s, \mu_t) = \left(\operatorname{argmin}_{\gamma \in \mathcal{B}} \sum_{i,j} \gamma_{i,j} \|\mathbf{h}_S(x_i) - \mathbf{h}_T(x_j)\|_p \right)^{\frac{1}{p}}, \quad (9)$$

where we opt for $p = 2$ and x_i, x_j are samples from \mathcal{X}_S and \mathcal{X}_T respectively. In other words, Equation. 9 is the loss function for feature alignment we consider when using OT method as opposed to the adversarial losses in Equations 2 and 3.

In a given setup, e.g. SIMBA and IllustrisTNG are in- and out-of-distribution datasets respectively, the pre-training phase is only run once, and an adaptation phase is run for each technique. For OT method, the learning rate used when adapting the target encoder for 200 epochs is 10^{-5} , and we resort to [51] in our implementation.

IV. RESULTS

A. SIMBA (IDs)→IllustrisTNG (OODs)

We first choose SIMBA HI and IllustrisTNG HI datasets to be the source and target domains respectively (SIMBA → TNG). It is worth reiterating that during the two training phases, pre-training and adaptation, the labels (Ω_m, σ_8) associated with the out-of-distribution maps (IllustrisTNG) are not used at all. The latter are only used to validate the predictions of the adapted encoder \mathbf{h}_T .

To evaluate the accuracy of our model predictions, we select the coefficient of determination R^2 which explains both the variance of the predicted parameters and the strength of correlation between the ground truth and prediction. We have that

$$R^2 = 1 - \frac{\sum_{i=1}^n (\theta_i - \mu_i)^2}{\sum_{i=1}^n (\theta_i - \bar{\theta})^2}, \quad (10)$$

where n and $\bar{\theta}$ are the number of samples in the test set and mean of the ground truth respectively. We present in Table I first row the performance of the model for the scenario SIMBA→TNG. Results show that the source network⁶ (i.e. $\mathbf{h}_S + \mathcal{R}_S$) is able to constrain the matter density to a good accuracy with $R^2 = 0.948$ on in-distribution maps. Although predicting σ_8 seems more challenging, the deep regressor still achieves $R^2 = 0.72$. This can be accounted for by the fact that the HI maps are more sensitive to matter density, as neutral hydrogen and dark matter are directly related via the bias, i.e. $\delta_{\text{HI}} \sim b_{\text{HI}} \delta_m$. We make predictions on the out-of-distribution images (IllustrisTNG) using the pre-trained source network to

⁶ It is worth making the distinction between network and encoder in the text. The former is the latter, which is the feature extractor, combined with the regressor.

TABLE I. R^2 score achieved on Ω_m and σ_8 from predicting the source and target datasets using the source and trained target network respectively. SN and TN denote source and target networks respectively. IDs and OODs in the table refer to in-distribution (source) and out-of-distribution (target) samples. Parameter inference improves significantly after adaptation (see SN (OODs) vs TN (OODs) columns).

	SN (IDs)		SN (OODs)		TN ^{ADDA} (OODs)		TN ^{OT} (OODs)	
	Ω_m	σ_8	Ω_m	σ_8	Ω_m	σ_8	Ω_m	σ_8
SIMBA→TNG	0.948	0.720	-0.474	-2.481	0.945	0.735	0.947	0.394
TNG→SIMBA	0.974	0.884	-2.109	-2.112	0.903	0.205	0.924	-0.215

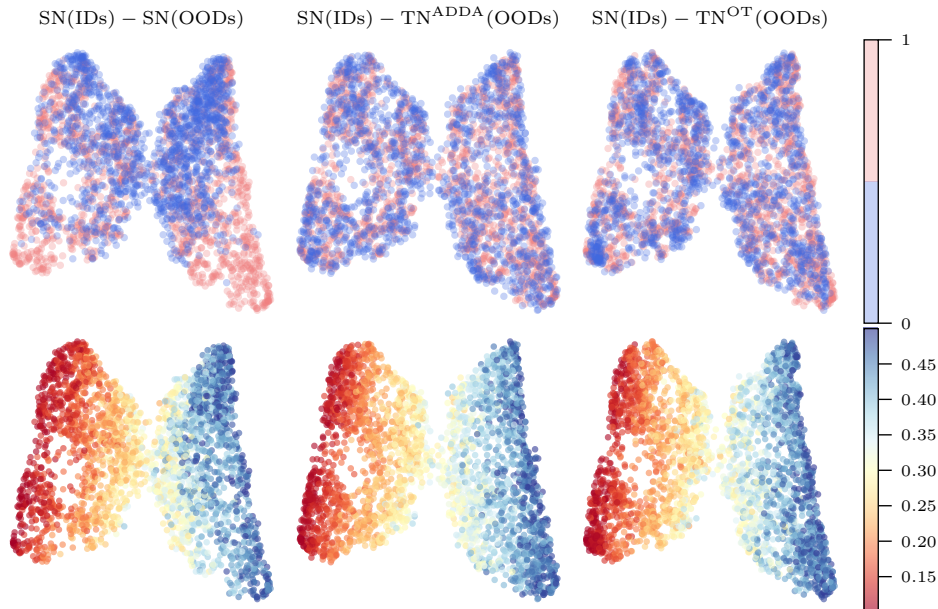


FIG. 4. The source and target datasets are SIMBA and IllustrisTNG respectively. 2D visualization of the features extracted by the source and target encoders using UMAP. *Top row*: in all panels the red dots denote the representations of in-distribution maps. The blue dots in first, second and third panels indicate the representations of the target dataset learned by source encoder, trained target encoder using ADDA and trained target encoder using optimal transport respectively. It can be clearly noticed that the representations are well aligned after adaptation. *Bottom row*: each panel in upper row is plotted again but using the corresponding value of Ω_m for the color coding.

TABLE II. R^2 score achieved on Ω_m and σ_8 similar to Table I but results are obtained from adapting the target encoder by using only 100 instances from the target domain.

	TN ^{ADDA} (OODs)		TN ^{OT} (OODs)	
	Ω_m	σ_8	Ω_m	σ_8
SIMBA→TNG	0.891	0.616	0.895	0.611
TNG→SIMBA	0.698	0.111	0.692	0.299

check how much the data shift impacts its performance and find that it fails to recover the cosmology, with $R^2 = -0.474$, -2.481 for Ω_m and σ_8 respectively. After adaptation, the target encoder is used to predict the cosmology of HI IllustrisTNG maps. Using ADDA method for the feature alignment, the target network TN^{ADDA} (i.e. $h_T + \mathcal{R}_S$) achieves very promising performance on the test set from the target domain – $R^2 = 0.945$, 0.735 on Ω_m and σ_8 respectively – similar to that of the source network on HI SIMBA maps (see Table I first row). This demonstrates the robustness of the adaptation technique which does not access the labels of the out-of-distribution

dataset at all during the training and uses the regressor \mathcal{R}_S pre-trained on the source domain for inference. On the other hand, the adapted network TN^{OT}, whose feature alignment is achieved using optimal transport, constrains the matter density on the target domain to a precision comparable to that of the source network on the source domain, but fails to extract the amplitude of the density fluctuations, $R^2 = 0.394$ on σ_8 . This indicates that in this specific scenario, SIMBA→TNG, ADDA method is more robust than the optimal transport.

We plot in Figure 4 the features extracted by the source and the two adapted encoders from the HI SIMBA and HI IllustrisTNG maps respectively. For this two dimensional visualization, we opt for UMAP method [52]. On the top row of Figure 4, red and blue dots denotes instances from in- and out-of-distribution datasets respectively. In the leftmost panel, we show representations of both SIMBA and IllustrisTNG maps extracted by the pre-trained source encoder h_T . The shift in latent space between the source and target domains is noticeable. After adaptation of the target encoder h_T , using either of the two methods (ADDA, optimal transport), the representations of SIMBA and IllustrisTNG obtained from h_S and h_T

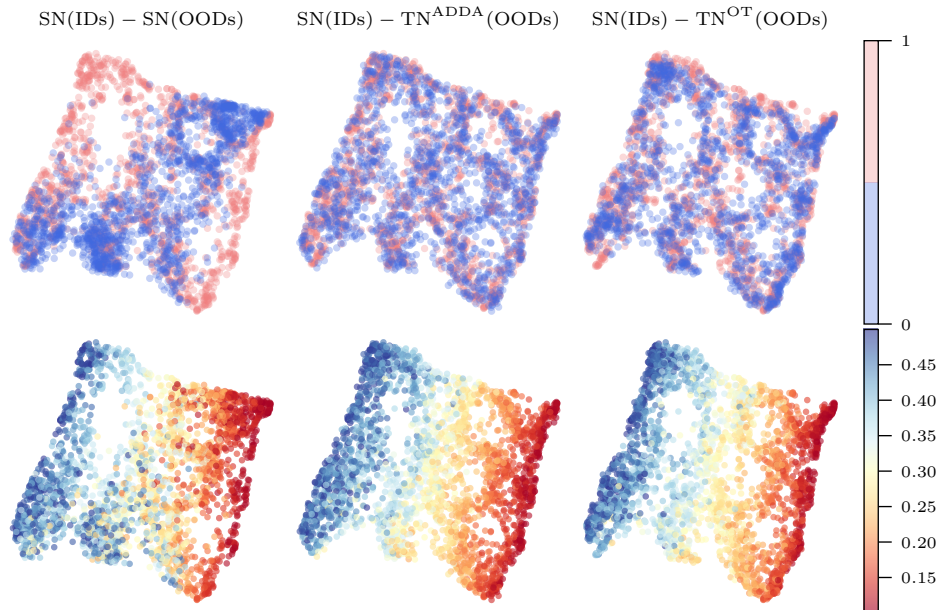


FIG. 5. Similar to what is shown in Figure 4 but the source and target datasets are IllustrisTNG and SIMBA respectively. The top panels show that there is a good overlap between the two representations after adaptation.

respectively are well aligned (see Figure 4 middle and right-most panels) as expected. This explains the reason why the regressor \mathcal{R}_S pre-trained on the source domain is able to predict the underlying matter density of the test set from the out-of-distribution dataset. Each panel at the bottom row of Figure 4 is the same as the corresponding one at the top row but the color coding is based on the value of Ω_m which is used for illustration here, given that the constraints obtained on it are tighter. The difference between the leftmost panel and the other two is that the color gradient is more pronounced in the latter, indicating that the instances whose Ω_m values are similar are well clustered in latent space. This trend also accounts for the fact that the maps are sensitive to the matter density.

B. IllustrisTNG (IDs)→SIMBA (OODs)

We now investigate the case where IllustrisTNG is considered as the source domain and SIMBA the target one (TNG→SIMBA). After pre-training, results show that the source network outperforms the one in SIMBA→TNG case, as evidenced by its accuracy to recover the cosmological parameters with $R^2 = 0.974, 0.884$ for Ω_m and σ_8 respectively (see also Table I second row). The constraint on σ_8 appears to be much tighter. The source network is also tested on the out-of-distribution examples and fails to constrain the underlying cosmology, as indicated by $R^2 = -2.109, -2.112$ on Ω_m and σ_8 respectively, as expected. We argue that the better performance of the source network to retrieve information from IllustrisTNG maps compared to those of SIMBA (during pre-training) is that the former exhibit much more details at high frequency modes (i.e. small scales) which also carry relevant

information (see Figure 1). We find that, irrespective of the feature alignment method used (ADDA, optimal transport), the adopted encoder h_T is able to constrain Ω_m but fails to constrain σ_8 from SIMBA maps (see Table I). The Ω_m predictions on out-of-distribution samples by trained h_T also appear to be slightly less precise than those obtained from the h_S on in-distribution instances, in contrast with the results that we have arrived at in the SIMBA→TNG scenario. The overall somewhat underperformance of h_T in the TNG→SIMBA case can be explained by the blurriness of the SIMBA maps on small scales which are relevant in order to extract the information about matter clustering that is directly related to σ_8 . The challenge posed by extracting information from SIMBA as the target domain is the reason why the adaptation is run for more epochs.

The trends, corresponding to the TNG→SIMBA case, exhibited in Figure 5 are similar to those highlighted in Figure 4. There is an overlap, hence a good alignment, between representations of the source and target domains after adaptation of the target encoder h_T , as shown in the top row of Figure 5. The clustering of instances corresponding to similar Ω_m values are also more apparent when representations of the out-of-distribution test set obtained from trained h_T are shown together with those of the in-distribution test set (see bottom row panels in Figure 5).

C. Can we adapt the target encoder using fewer instances?

In a real world scenario, at an early stage of an HI experiment, we do not expect to collect thousands of maps for training a deep learning model. We therefore investigate the idea

of adapting the target encoder using relatively small instances from the target domain. We adapt the target encoder using the two adaptation techniques in each setup, i.e. SIMBA→TNG and TNG→SIMBA, as before. The hyperparameters in each setup for each technique are the same as those considered to arrive at the results presented in §IV A and §IV B. For this test, we select 100 instances from the target domain to train the target encoder. The cosmological predictions on out-distribution instances are presented in Table II. It is clear that the constraints on the matter density are tighter than those of the amplitude of the density fluctuations in all cases. In each setup, the accuracy of the adapted network to extract the cosmological information from the target domain maps remains roughly the same using either ADDA or OT. On the one hand, the trained target network is still able to recover Ω_m from the out-of-distribution maps in SIMBA→TNG with a precision of $R^2 = 0.891$ despite the relatively small number of instances used to adapt it, about two orders of magnitude smaller than the training dataset used in §IV A (12,000 examples). This provides further insights into the robustness of the techniques considered in this work. On the other hand, extracting the underlying matter density from the out-of-distribution maps in TNG→SIMBA poses a challenge to the adapted network, consistent with the trend which has already been highlighted in §IV B. Regardless of the approach used, the trained target network achieves an $R^2 \sim 0.69$ on Ω_m overall.

V. CONCLUSIONS

We have shown in this work that extracting cosmological information from out-of-distribution HI maps is feasible by utilizing unsupervised domain adaptation techniques. We have considered SIMBA and IllustrisTNG HI maps, which are generated by two dissimilar distributions, owing to their own treatment of baryon physics. After pre-training a source network, composed of an encoder and a regressor, on the in-distribution dataset, the source encoder weights serve as initial weights of a target encoder with identical architecture. We have opted for two different methods to align the features from the two domains in a lower dimension embedding space; an adversarial approach, Adversarial Discriminative Domain Adaptation (ADDA), which resorts a discriminator that differentiates the representations of the source domain from those of the target domain through the training, and optimal transport which consists of minimizing the Wasserstein distance between the two representations. We note that the out-of-distribution dataset is assumed to be unlabeled, in other words its labels (the cosmological parameters) are not accessed during the adaptation phase and the regressor, pre-trained along with the source encoder on the source domain, is directly used in combination with the adapted target encoder for inference on the test set from the target domain. The labels of the target domain are only utilized to evaluate the performance of the trained target encoder. We consider two scenarios where SIMBA and IllustrisTNG are the source and target domains respectively, i.e. SIMBA→TNG, and vice versa, i.e. TNG→SIMBA.

We find that in the SIMBA→TNG case, the target encoder, which has been adapted using ADDA, achieves a performance comparable to that of the source encoder on the source domain. The prediction accuracies of the source network on Ω_m and σ_8 are $R^2 = 0.948$ and 0.720 respectively on HI SIMBA dataset, whereas the trained target network achieves $R^2 = 0.945, 0.735$ (Ω_m, σ_8) on IllustrisTNG HI maps. When using optimal transport for feature alignment, the target encoder fares equally well in terms of recovering Ω_m from the HI IllustrisTNG maps, but fails to extract the amplitude of the density fluctuations σ_8 . When cast into a two dimension subspace for visualization, the two representations of both source and target domains overlap well after feature alignment, as expected. Results show that, regardless of the adaptation method considered for the feature alignment, only the matter density can be retrieved from the out-of-distribution maps in the TNG→SIMBA case. Extracting the amplitude of density fluctuations from the SIMBA maps proves to be quite challenging.

In the SIMBA→TNG case, the weights of the pre-trained h_S are optimized to recover the cosmology from (relatively) blurry maps and are used to initialize the weights of h_T that are updated through feature alignment in order to predict the cosmology from more detailed maps of the target domain, i.e. IllustrisTNG. It is possible for the trained h_T to achieve a performance comparable to that of the source network, as indicated by the results in Table I. However, in the TNG→SIMBA scenario, weights that are trained to retrieve information from relatively detailed source domain maps are transferred to target encoder weights that are adapted to infer cosmological parameters from target domain maps with less information in the high frequency modes. This makes the adaptation task more challenging, hence the asymmetry of the results from the two scenarios.

We have also explored the idea of utilizing relatively small dataset from the target domain, about 100 times smaller than the original target domain dataset in each setup, to adapt the target encoder. It has been found that, regardless of the size of the training samples used for the adaptation, the trained target network is still able to predict the matter density to a reasonable accuracy, $R^2 \sim 0.89$, from IllustrisTNG HI maps in the SIMBA→TNG setup. Extracting Ω_m from SIMBA in TNG→SIMBA, however, proves to be difficult.

As the HI data that will be collected in the near future from various experiments will be unlabeled, the proof of concept described in this work plays a key role in terms of optimizing the information extraction from the maps. For future work, we will investigate the use of other more sophisticated technique such as Cycle-consistent adversarial domain adaptation (Cycada) [53], in order to further improve the robustness of the parameter inference on out-of-distribution samples. It is worth noting that our approach can be easily exploited for retrieving information from other large scale observables.

ACKNOWLEDGMENTS

SA acknowledges financial support from the *South African Radio Astronomy Observatory* (SARAO). SH acknowledges support for Program number HST-HF2-51507 provided by

NASA through a grant from the Space Telescope Science Institute, which is operated by the Association of Universities for Research in Astronomy, incorporated, under NASA contract NAS5-26555. The CAMELS project is supported by the Simons Foundation and NSF grant AST 2108078.

-
- [1] R. A. Battye, R. D. Davies, and J. Weller, Neutral hydrogen surveys for high-redshift galaxy clusters and protoclusters, *Monthly Notices of the Royal Astronomical Society* **355**, 1339 (2004).
- [2] T.-C. Chang, U.-L. Pen, J. B. Peterson, and P. McDonald, Baryon acoustic oscillation intensity mapping of dark energy, *Physical Review Letters* **100**, 091303 (2008).
- [3] P. Bull, P. G. Ferreira, P. Patel, and M. G. Santos, Late-time cosmology with 21 cm intensity mapping experiments, *The Astrophysical Journal* **803**, 21 (2015).
- [4] A. Pourtsidou, D. Bacon, and R. Crittenden, H_i and cosmological constraints from intensity mapping, optical and cmb surveys, *Monthly Notices of the Royal Astronomical Society* **470**, 4251 (2017).
- [5] G. Mellema, L. V. Koopmans, F. A. Abdalla, G. Bernardi, B. Ciardi, S. Daiboo, A. de Bruyn, K. K. Datta, H. Falcke, A. Ferrara, *et al.*, Reionization and the cosmic dawn with the square kilometre array, *Experimental Astronomy* **36**, 235 (2013).
- [6] R. Battye, I. Browne, C. Dickinson, G. Heron, B. Maffei, and A. Pourtsidou, H_i intensity mapping: a single dish approach, *Monthly Notices of the Royal Astronomical Society* **434**, 1239 (2013).
- [7] K. Bandura, G. E. Addison, M. Amiri, J. R. Bond, D. Campbell-Wilson, L. Connor, J.-F. Cliche, G. Davis, M. Deng, N. Denman, *et al.*, Canadian hydrogen intensity mapping experiment (chime) pathfinder, in *Ground-based and Airborne Telescopes V*, Vol. 9145 (SPIE, 2014) pp. 738–757.
- [8] M.-A. Bigot-Sazy, Y.-Z. Ma, R. A. Battye, I. W. Browne, T. Chen, C. Dickinson, S. Harper, B. Maffei, L. C. Olivari, and P. N. Wilkinson, H_i intensity mapping with fast, arXiv:1511.03006 (2015).
- [9] Y. Li, Y. Wang, F. Deng, W. Yang, W. Hu, D. Liu, X. Zhao, S. Zuo, S. Shu, J. Li, *et al.*, Fast drift scan survey for H_i intensity mapping: I. preliminary data analysis, *The Astrophysical Journal* **954**, 139 (2023).
- [10] D. R. DeBoer, A. R. Parsons, J. E. Aguirre, P. Alexander, Z. S. Ali, A. P. Beardsley, G. Bernardi, J. D. Bowman, R. F. Bradley, C. L. Carilli, *et al.*, Hydrogen epoch of reionization array (hera), *Publications of the Astronomical Society of the Pacific* **129**, 045001 (2017).
- [11] M. G. Santos, M. Cluver, M. Hilton, M. Jarvis, G. I. Jozsa, L. Leeuw, O. Smirnov, R. Taylor, F. Abdalla, J. Afonso, *et al.*, MeerKAT: MeerKAT large area synoptic survey, arXiv:1709.06099 (2017).
- [12] B. Greig and A. Mesinger, 21cmMC: an MCMC analysis tool enabling astrophysical parameter studies of the cosmic 21 cm signal, *Monthly Notices of the Royal Astronomical Society* **449**, 4246 (2015).
- [13] S. Hassan, R. Davé, K. Finlator, and M. G. Santos, Epoch of reionization 21 cm forecasting from MCMC-constrained semi-numerical models, *Monthly Notices of the Royal Astronomical Society* **468**, 122 (2017).
- [14] S. Bharadwaj and S. K. Pandey, Probing non-gaussian features in the H_i distribution at the epoch of re-ionization, *Monthly Notices of the Royal Astronomical Society* **358**, 968 (2005).
- [15] S. Majumdar, J. R. Pritchard, R. Mondal, C. A. Watkinson, S. Bharadwaj, and G. Mellema, Quantifying the non-gaussianity in the eor 21-cm signal through bispectrum, *Monthly Notices of the Royal Astronomical Society* **476**, 4007 (2018).
- [16] L. F. Randrianjanahary, D. Karagiannis, and R. Maartens, Cosmological constraints from the eor 21-cm power spectrum and tree-level bispectrum of 21 cm intensity maps, *Physics of the Dark Universe* **45**, 101530 (2024).
- [17] N. Gillet, A. Mesinger, B. Greig, A. Liu, and G. Ucci, Deep learning from 21-cm tomography of the cosmic dawn and reionization, *Monthly Notices of the Royal Astronomical Society* **484**, 282 (2019).
- [18] S. Hassan, F. Villaescusa-Navarro, B. Wandelt, D. N. Spergel, D. Anglés-Alcázar, S. Genel, M. Cranmer, G. L. Bryan, R. Davé, R. S. Somerville, *et al.*, Hiflow: Generating diverse H_i maps and inferring cosmology while marginalizing over astrophysics using normalizing flows, *The Astrophysical Journal* **937**, 83 (2022).
- [19] F. Villaescusa-Navarro, D. Anglés-Alcázar, S. Genel, D. N. Spergel, R. S. Somerville, R. Dave, A. Pillepich, L. Hernquist, D. Nelson, P. Torrey, *et al.*, The camels project: Cosmology and astrophysics with machine-learning simulations, *The Astrophysical Journal* **915**, 71 (2021).
- [20] G. Papamakarios, T. Pavlakou, and I. Murray, Masked autoregressive flow for density estimation, *Advances in neural information processing systems* **30** (2017).
- [21] S. Andrianomena and S. Hassan, Predictive uncertainty on astrophysics recovery from multifield cosmology, *Journal of Cosmology and Astroparticle Physics* **2023** (06), 051.
- [22] S. Hassan, S. Andrianomena, and C. Doughty, Constraining the astrophysics and cosmology from 21 cm tomography using deep learning with the ska, *Monthly Notices of the Royal Astronomical Society* **494**, 5761 (2020).
- [23] A. Liu, M. Tegmark, J. Bowman, J. Hewitt, and M. Zaldarriaga, An improved method for 21-cm foreground removal, *Monthly Notices of the Royal Astronomical Society* **398**, 401 (2009).
- [24] A. Liu and M. Tegmark, A method for 21 cm power spectrum estimation in the presence of foregrounds, *Physical Review D—Particles, Fields, Gravitation, and Cosmology* **83**, 103006 (2011).
- [25] D. Alonso, P. Bull, P. G. Ferreira, and M. G. Santos, Blind foreground subtraction for intensity mapping experiments, *Monthly Notices of the Royal Astronomical Society* **447**, 400 (2015).
- [26] S. Wold, K. Esbensen, and P. Geladi, Principal component analysis, *Chemometrics and intelligent laboratory systems* **2**, 37 (1987).
- [27] T. L. Makinen, L. Lancaster, F. Villaescusa-Navarro, P. Melchior, S. Ho, L. Perreault-Levasseur, and D. N. Spergel, deep21: a deep learning method for 21 cm foreground removal, *Journal of Cosmology and Astroparticle Physics* **2021** (04), 081.
- [28] Y. Ganin and V. Lempitsky, Unsupervised domain adaptation

- by backpropagation, in *International conference on machine learning* (PMLR, 2015) pp. 1180–1189.
- [29] B. Sun and K. Saenko, Deep coral: Correlation alignment for deep domain adaptation, in *Computer Vision—ECCV 2016 Workshops: Amsterdam, The Netherlands, October 8–10 and 15–16, 2016, Proceedings, Part III 14* (Springer, 2016) pp. 443–450.
- [30] K. Bousmalis, G. Trigeorgis, N. Silberman, D. Krishnan, and D. Erhan, Domain separation networks, *Advances in neural information processing systems* **29** (2016).
- [31] M. Dell’Aiera, T. Vuillaume, M. Jacquemont, and A. Benoit, Deep unsupervised domain adaptation applied to the cherenkov telescope array large-sized telescope, in *Proceedings of the 20th International Conference on Content-based Multimedia Indexing* (2023) pp. 133–139.
- [32] A. Ćiprijanović, A. Lewis, K. Pedro, S. Madireddy, B. Nord, G. N. Perdue, and S. M. Wild, Deepastrouda: semi-supervised universal domain adaptation for cross-survey galaxy morphology classification and anomaly detection, *Machine Learning: Science and Technology* **4**, 025013 (2023).
- [33] A. Ćiprijanovic, D. Kafkes, G. F. Snyder, F. J. Sánchez, G. N. Perdue, K. Pedro, B. Nord, S. Madireddy, and S. M. Wild, Deepadversaries: examining the robustness of deep learning models for galaxy morphology classification., *Mach. Learn. Sci. Technol.* **3**, 35007 (2022).
- [34] S. Gilda, A. de Mathelin, S. Bellstedt, and G. Richard, Unsupervised domain adaptation for constraining star formation histories (2024).
- [35] M. Sugiyama, S. Nakajima, H. Kashima, P. Buenau, and M. Kawanabe, Direct importance estimation with model selection and its application to covariate shift adaptation, *Advances in neural information processing systems* **20** (2007).
- [36] A. Ćiprijanović, D. Kafkes, S. Jenkins, K. Downey, G. N. Perdue, S. Madireddy, T. Johnston, and B. Nord, Domain adaptation techniques for improved cross-domain study of galaxy mergers, arXiv:2011.03591 (2020).
- [37] A. J. Smola, A. Gretton, and K. Borgwardt, Maximum mean discrepancy, in *13th international conference, ICONIP* (2006) pp. 3–6.
- [38] F. Villaescusa-Navarro, S. Genel, D. Angles-Alcazar, L. Thiele, R. Dave, D. Narayanan, A. Nicola, Y. Li, P. Villanueva-Domingo, B. Wandelt, *et al.*, The camels multifield data set: Learning the universe’s fundamental parameters with artificial intelligence, *The Astrophysical Journal Supplement Series* **259**, 61 (2022).
- [39] F. Villaescusa-Navarro, S. Genel, D. Anglés-Alcázar, L. A. Perez, P. Villanueva-Domingo, D. Wadekar, H. Shao, F. G. Mohammad, S. Hassan, E. Moser, *et al.*, The camels project: public data release, arxiv:2201.01300 (2022).
- [40] D. Nelson, V. Springel, A. Pillepich, V. Rodriguez-Gomez, P. Torrey, S. Genel, M. Vogelsberger, R. Pakmor, F. Marinacci, R. Weinberger, *et al.*, The illustriTng simulations: public data release, *Computational Astrophysics and Cosmology* **6**, 1 (2019).
- [41] R. Davé, D. Anglés-Alcázar, D. Narayanan, Q. Li, M. H. Rafieferantsoa, and S. Appleby, Simba: Cosmological simulations with black hole growth and feedback, *Monthly Notices of the Royal Astronomical Society* **486**, 2827 (2019).
- [42] F. Haardt and P. Madau, Radiative transfer in a clumpy universe. iv. new synthesis models of the cosmic uv/x-ray background, *The Astrophysical Journal* **746**, 125 (2012).
- [43] C.-A. Faucher-Giguere, A. Lidz, M. Zaldarriaga, and L. Hernquist, A new calculation of the ionizing background spectrum and the effects of he ii reionization, *The Astrophysical Journal* **703**, 1416 (2009).
- [44] A. Farahani, S. Voghoei, K. Rasheed, and H. R. Arabnia, A brief review of domain adaptation, *Advances in data science and information engineering: proceedings from ICDATA 2020 and IKE 2020*, 877 (2021).
- [45] E. Tzeng, J. Hoffman, K. Saenko, and T. Darrell, Adversarial discriminative domain adaptation, in *Proceedings of the IEEE conference on computer vision and pattern recognition* (2017) pp. 7167–7176.
- [46] K. Simonyan and A. Zisserman, Very deep convolutional networks for large-scale image recognition, arXiv preprint arXiv:1409.1556 (2014).
- [47] N. Courty, R. Flamary, D. Tuia, and A. Rakotomamonjy, Optimal transport for domain adaptation, *IEEE transactions on pattern analysis and machine intelligence* **39**, 1853 (2016).
- [48] L. Kantorovitch, On the translocation of masses, *Management science* **5**, 1 (1958).
- [49] N. Bonneel, M. Van De Panne, S. Paris, and W. Heidrich, Displacement interpolation using lagrangian mass transport, in *Proceedings of the 2011 SIGGRAPH Asia conference* (2011) pp. 1–12.
- [50] Y. Rubner, C. Tomasi, and L. J. Guibas, The earth mover’s distance as a metric for image retrieval, *International journal of computer vision* **40**, 99 (2000).
- [51] R. Flamary, N. Courty, A. Gramfort, M. Z. Alaya, A. Boissunon, S. Chambon, L. Chapel, A. Corenflos, K. Fatras, N. Fournier, *et al.*, Pot: Python optimal transport, *Journal of Machine Learning Research* **22**, 1 (2021).
- [52] L. McInnes, J. Healy, and J. Melville, Umap: Uniform manifold approximation and projection for dimension reduction, arXiv preprint arXiv:1802.03426 (2018).
- [53] J. Hoffman, E. Tzeng, T. Park, J.-Y. Zhu, P. Isola, K. Saenko, A. Efros, and T. Darrell, Cycada: Cycle-consistent adversarial domain adaptation, in *International conference on machine learning* (Pmlr, 2018) pp. 1989–1998.